ACS OMEGA

http://pubs.acs.org/journal/acsodf

Article

Study on the Ways to Improve the CO_2–H_2O Displacement Efficiency in Heterogeneous Porous Media by Lattice Boltzmann Simulation

Ling Ren,* Qi Liu, Yang Ni, Yucong Xia, and Jianguo Chen

Cite This: *ACS Omega* 2022, 7, 20833–20844

Read Online

ACCESS | Metrics & More | Article Recommendations

ABSTRACT: To improve the efficiency of CO_2 geological sequestration, it is of great significance to in-depth study the physical mechanism of the immiscible CO_2–water displacement process, where the influential factors can be divided into fluid–fluid and fluid–solid interactions and porous media characteristics. Based on the previous studies of the interfacial tension (capillary number) and viscosity ratio factors, we conduct a thorough study about the effects of fluid–solid interaction (i.e., wettability) and porous media characteristics (i.e., porosity and non-uniformity of granule size) on the two-phase displacement process by constructing porous media with various structural parameters and using a multiphase lattice Boltzmann method. The displacement efficiency of CO_2 is evaluated by the breakthrough time characterizing the displacement speed and the quasi-steady state saturation representing the displacement amount. It is shown that the breakthrough time of CO_2 becomes longer, but the quasi-steady state saturation increases markedly with the increase in CO_2 wettability with the surface, demonstrating an overall improvement of the displacement efficiency. Furthermore, the breakthrough time of CO_2 shortens and the saturation increases significantly with increasing porosity, granule size, and non-uniformity, showing the improvement of the displacement efficiency. Therefore, enhancing the wettability of CO_2 with the surface and selecting reservoirs with greater porosity, larger granule size, and non-uniformity can all contribute to the efficiency improvement of CO_2 geological sequestration.

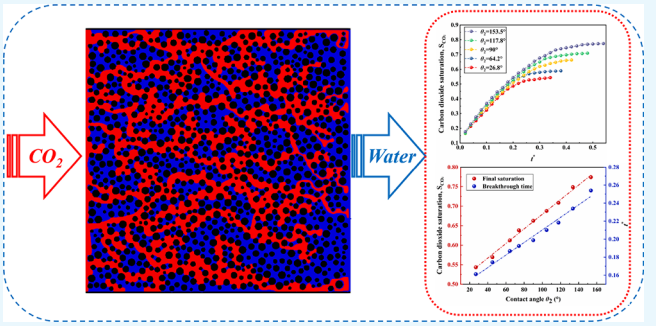

1. INTRODUCTION

CCS (carbon capture and sequestration) is currently recognized as an effective technology that directly reduces CO_2 emissions worldwide.[1−3] Injection of CO_2 into deep saline aquifers is known to be the most feasible option for carbon storage, which has the maximum accessibility and highest storage capacity.[4−7] Under the conditions of typical underground saline aquifers, CO_2 usually remains in the supercritical state or liquid state.[8] When CO_2 is injected into deep saline aquifers, it displaces the formation fluid from the pore space in a complex pattern dominated by capillary and viscous forces, as well as geological heterogeneities. It is of great significance to in-depth study the physical mechanism of immiscible multiphase flow to evaluate the storage capacity of saline aquifers and improve the efficiency of CO_2 geological sequestration.

For the immiscible two-phase displacement process in porous media, the influencing factors can be divided into fluid–fluid and fluid–solid interactions and porous media characteristics.

The influencing factors on the fluid–fluid interaction mainly include the viscosity ratio, interfacial tension (capillary number), and density ratio between the two-phase fluids. For the displacement of water by CO_2, the viscosity ratio and capillary number are the main influencing factors.[9] The capillary number characterizes the relationship between viscous force and interfacial tension, defined as $Ca = (\eta u)/\gamma$, where η, u, and γ are the dynamic viscosity, inlet velocity, and interfacial tension of the fluid, respectively. The viscosity ratio between two fluids is defined as $M = \mu_2/\mu_1$, where μ_2 and μ_1 are the dynamic viscosities of the invading fluid and the displaced one, respectively. With the increase in Ca or decrease in M, the capillary pressure is reduced during the flow, which helps stabilize the displacement front surface, allows the invading fluid to invade more pores, and thus improves the displacement efficiency.[10−14]

In the process of displacement, immiscible fluids will adhere to the solid surface of the porous media and produce competition, manifesting by the wettability of the coupling between the fluid–fluid interface and the solid surface, i.e., the

Received: March 10, 2022
Accepted: May 30, 2022
Published: June 9, 2022

contact angle.[15−17] Previous studies include the influence of wettability on the evolution process of the phase interface, relative permeability, and displacement efficiency.[18−24] The increase in invading fluid wettability yields a cooperative pore-filling mechanism and stabilizes the immersion mode, which inhibits fingering to a certain extent and improves the relative permeability and displacement efficiency of the invading fluid.

The porous media characteristic factors mainly include porosity, skeleton structure, granule size, tortuosity, permeability, and specific surface area.[25] Among them, the porosity, skeleton structure, and granule size are the dominant factors that determine the tortuosity, permeability, and other factors of the porous media. Scholars systematically discuss the flow characteristics and displacement efficiency of two-phase flow under various porosities.[26] With the increase in porosity, the invading fluid becomes much more continuous during the flow with higher saturation in the quasi-steady state. However, different skeleton structures also affect the displacement process significantly even under a constant porosity. Obviously, porosity alone cannot accurately describe the structural characteristics of porous media. A combination of CT (computerized tomography) scan and numerical reconstruction is used to characterize the skeleton structure of real porous media samples for studying the displacement behavior.[27,28] However, the results are only applicable to specific pore structures, and it is hard to obtain the general law about the influence of a single factor on the displacement. Considering both the porosity and skeleton structure, an effective method is to simplify complex structures of porous media to definite geometric shapes.[29] For example, when the skeleton structure is numerically constructed by circles as granules, it is found that the overall displacement law is basically similar to the one of real porous media.[30,31] In view of the influence of granule size on the displacement process and efficiency, it is generally carried out in homogeneous porous media.[9] However, real porous media are often heterogeneous where the granule size is non-uniform and the ranges are also different, which is rarely studied.

In summary, the factors of the fluid−fluid interaction have been more comprehensively studied, such as the capillary number. However, the research on the factors affecting the fluid−solid interaction is not comprehensive enough, which needs to be further studied, including the wettability of CO_2 to the solid surface. Furthermore, the study of the influencing factors of the porous media characteristics in the heterogeneous case is less, i.e., non-uniform granule size.

The researchers use a variety of methods to study the two-phase displacement process, including experiments and numerical simulations. Due to the limitation of experimental conditions, numerical simulation is much more effective in predicting multiphase flow in porous media and supplementing experimental conditions. Compared with other numerical methods, the LBM (lattice Boltzmann method) at mesoscopic scales, which can handle various complex geometric boundaries and accurately capture the evolution of phase interfaces, has great advantages in solving complex fluid flow problems.[32−35] Therefore, the LBM is applied to investigate the influence of fluid−solid interaction and porous media characteristics on the immiscible two-phase displacement process and efficiency, specifically including the wettability, porosity, granule size, and non-uniformity of the heterogeneous porous media.

2. NUMERICAL METHOD

2.1. Multiphase Lattice Boltzmann Method. The SCMC-LBM (Shan-Chen Multicomponent-LBM) model has been widely used in multiphase flow in porous media.[35−40] In the present study, the two-phase flow of immiscible fluids is modeled using the SCMC-LBM model. A two-dimensional D2Q9[37] is considered. The particle distribution functions satisfying the lattice Boltzmann equation are introduced for each fluid phase.[36,37,41] The fluids are subjected to the combined action of external forces during the flow, including the body force $\mathbf{G}^{\sigma}$, the interaction forces $\mathbf{F}_{ads}^{\sigma}$ between fluid and solid, and $\mathbf{F}_{c}^{\sigma}$ between fluid and fluid.[33,42,43]

2.2. Initial and Boundary Conditions. The computational domain is 500 × 500 lu^2 (lu: lattice unit), where CO_2 is injected from the left side and outflows through the right side. At the initial time, the pore space of the calculation domain (0−1 lu) is filled with CO_2 and of the rest with water, both with zero initial velocities. The inlet velocity and outlet pressure boundary conditions are given by Zou−He relations,[44,45] where the nonzero inlet velocity is u_x in the flow direction. The nonslip bounce-back boundaries are applied to the top, bottom, and internal skeleton structure of porous media.[46]

2.3. Samples of Porous Media. For the two-phase flow, the bounce-back boundary condition used by the LBM method requires a certain number of lattices between solids, and too few lattices will lead to numerical instability, resulting in scattering or low accuracy.[24,26,47] Therefore, the minimum channel width in the physical model of porous media should be greater than four lattices.[24,26,48] As a result, the applicability of the LBM for the two-phase flow depends on the minimum channel width. Based on the above-mentioned requirement and the reconstruction method of the porous media in this paper, the solid granules are not in contact with each other so that the pore spaces are completely connected, and the porosity is limited to greater than 0.6 in the simulation. The flow mechanism with lower porosity could be inferred according to the numerical simulations.

The two-dimensional models of porous media are generated with the granules represented by circles.[6] The algorithm for generating porous media with a random structure can be described as follows: (1) the calculation domain, porosity, distance between circles, granule size types, and average granule size are given; (2) randomly generate the coordinates of the first circle center (x, y); (3) randomly generate the coordinates of the i-th $(i > 1)$ circle center (x_i, y_i) and judge whether the channel width is greater than four lattices; (4) determine whether the requirements of porosity and average granule size are met, and if not, repeat step (3); (5) repeat steps (3) and (4) until all the requirements are met, and output the results. The reconstruction rules are shown in Figure 1.

In this article, 15 samples of porous media with different structures are generated, whose structural features are shown in Table 1. The dimensionless parameters are applied for obtaining general laws. The dimensionless time is defined by $t^* = u_x t/ly$,[48] where ly is the width of the computational domain and set to 500 lu in the simulation. D is the granule size in lattice unit (lu), and the average granule size $\bar{D}$ is calculated by the average value of all the granule sizes. The dimensionless granule size and average granule size are defined by $D^* = D/ly$ and $\bar{D}^* = \bar{D}/ly$, respectively. It is assumed that

https://doi.org/10.1021/acsomega.2c01436
ACS Omega 2022, 7, 20833−20844

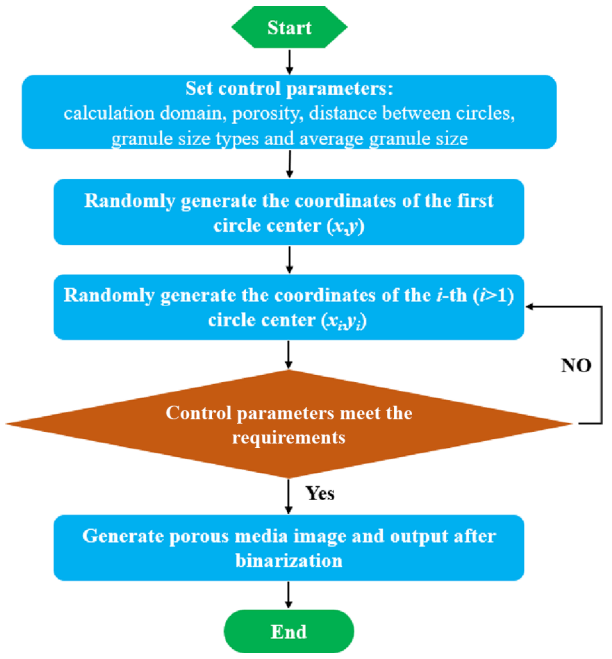

Figure 1. Flow chart for numerical reconstruction of heterogeneous porous media.

the 500 × 500 lu^2 computational domain corresponds to the physical size of 5 × 5 mm^2, with each lattice being 10 μm.[24,26] The permeability k, an inherent property of porous media independent of the properties of the fluid, is calculated by Darcy's law as $k = u_a \nu ly/\Delta p$, where u_a is the average velocity in the flow field, ν is the kinematic viscosity of the fluid, and Δp is the pressure difference at the inlet and outlet.

The 15 samples of porous media are presented in Table 1, where samples 1−5 contribute to the study of porosity factor for the same average granule size, samples 11−15 contribute to the study of uniform granule size factor for the same porosity, samples 3, 7, 8, 9, and 10 contribute to the study of average granule size factor for the same porosity, and samples 3, 6, and 11 contribute to the study of non-uniformity factor for the same porosity and average granule size.

Figure 2 visually shows the porous media structures of samples 1, 3, 6, and 11. By comparing the four samples,

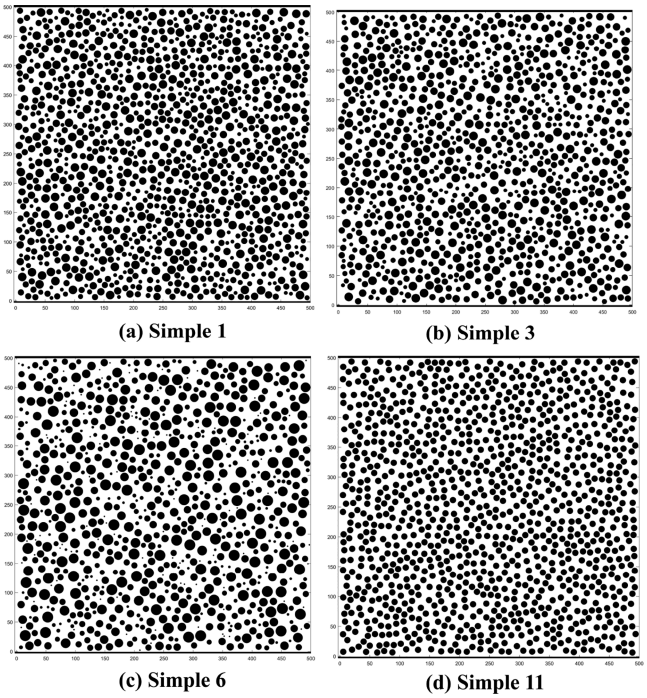

Figure 2. Visualization of the porous media model.

although the average granule sizes are the same, the porosity or granule size is different, manifesting various skeleton structures.

2.4. Model Validation. The basic code[49] is improved by adding the fluid−fluid force and fluid−solid force and correcting the equilibrium velocity of each fluid component based on the two forces through the C++ language in the Linux environment. The SCMC-LBM model is validated using two standard benchmarks tests: the Young−Laplace test and the static contact angle test.

2.4.1. The Young−Laplace Test. For the SCMC-LBM model, the interfacial tension γ between the two fluid components needs to be indirectly calculated using the droplet

Table 1. Characteristics of Porous Media

sample	porosity ε	granule size $D/(\mu m)$	dimensionless granule size range $D^* \times 10^3$	average granule size $\bar{D}/(\mu m)$	dimensionless average granule size $\bar{D}^*$	permeability $k/\mu m^2$
1	0.60	30, 40, 50, 60, 70	6, 8, 10, 12, 14	49.98	0.01	59.16
2	0.62			49.99		70.82
3	0.65			49.99		99.45
4	0.68			49.98		154.04
5	0.70			49.99		180.14
6	0.65	10, 20, 30, 40, 50, 60, 70, 80, 90	2, 4, 6, 8, 10, 12, 14, 16, 18	49.99		141.23
7	0.65	40−80	8, 10, 12, 14, 16	59.99	0.012	142.03
8	0.65	50−90	10, 12, 14, 16, 18	69.98	0.014	196.04
9	0.65	60−100	10, 12, 14, 16, 18, 20	79.98	0.016	254.77
10	0.65	70−110	14, 16, 18, 20, 22	89.97	0.018	335.79
11	0.65	50	10	50	0.01	93.28
12	0.65	60	12	60	0.012	126.47
13	0.65	70	14	70	0.014	174.10
14	0.65	80	16	80	0.016	222.59
15	0.65	90	18	90	0.018	304.61

https://doi.org/10.1021/acsomega.2c01436
ACS Omega 2022, 7, 20833−20844

model. The Young−Laplace test is to verify that the model developed can accurately determine the interfacial tension at various fluid−fluid interaction strength coefficients G_c.

The 200 × 200 lu^2 droplet model is established, where the periodic boundaries are applied in the x- and y-directions of the simulation domain. The G_c values are 0.8, 0.9, 1.0, and 1.1, respectively. Five different droplet radii are initialized as R_i = [20, 25, 30, 40, 50]. The density ratio of water to CO_2 is set to 1, and the viscosity ratios are set to 8. The relationship between the pressure difference across the interface and the final size of the droplet is determined, as shown in Figure 3.

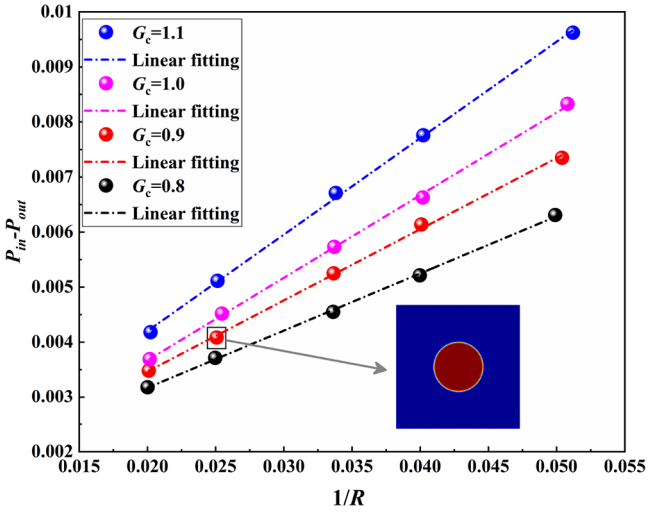

Figure 3. Relationship between ΔP and $1/R$.

The simulation results satisfy Laplace's law. The slope of the fitting line is the interfacial tension increasing with increasing fluid−fluid interaction strength coefficient G_c. As observed in Figure 3, the interfacial tension at different G_c values corresponds to 0.104, 0.128, 0.151, and 0.175.

2.4.2. The Static Contact Angle Test. The static contact angle test is to confirm that the established model can accurately determine the contact angle θ_σ between two fluid components and the solid surface under different fluid−solid interaction strength coefficients $G_{ads,\sigma}$.

A 300 × 200 lu^2 computational domain is selected in which supercritical CO_2 and water are placed above a solid surface and different wettability values are considered. The main and associated dissolved densities of both fluids are set to ρ_{main} = 2.0 and $\rho_{dissolve}$ = 0.06, respectively, and the G_c is 0.9. The half-step bounce-back boundary conditions (no-slip zero velocity) are implemented at the top and bottom walls and the periodic boundary conditions for both left and right boundaries.[33] Under the effect of interfacial tension and the interaction between the solid surface and the fluid components, the contact angle can be measured when the steady state of the fluids is finally reached.

Simulation results of three typical static contact angles are shown in Figure 4, where blue indicates supercritical CO_2 as fluid component 1 (σ = 1), and red indicates water as fluid component 2 (σ = 2). The contact angles formed at the bottom boundary for fluid components are labeled as θ_1 and θ_2, respectively. The two-phase fluid exhibits opposite wettability to the surface so that $\theta_1 + \theta_2 = 180°$. For water, the three typical simulations are as follows: (a) high, (b) neutral, and (c) low wetting, as demonstrated in Figure 4.

The relationship between the contact angle θ_2 and $G_{ads,2}$ is shown in Figure 5 for water. It is found that the simulation

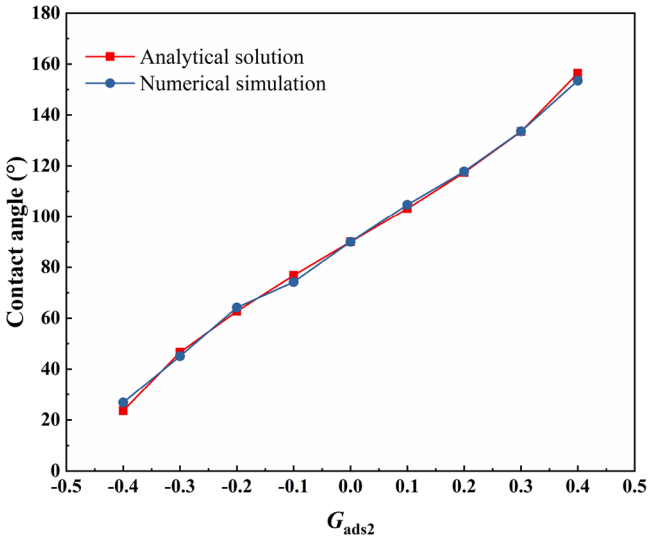

Figure 5. Relationship between $G_{ads,2}$ and contact angle θ_2.

results are in good agreement with the analytical solution proposed by Huang et al.,[33] i.e., $\cos\theta_2 = \frac{G_{ads,1} - G_{ads,2}}{G_c \frac{\rho_{main} - \rho_{dissolve}}{2}}$, demonstrating that the program developed can accurately describe the wettability of the fluids to the surface.

3. RESULTS AND DISCUSSION

During the simulation, the viscosity ratio M between water and CO_2 is 8, the inlet velocity u_x is supposed to be 10^{-3}, G_c and the corresponding interfacial tension γ are 0.9 and 0.128, respectively, and dynamic viscosity η_{CO_2} is 0.1. The study is carried out under Ca = 7.81 × 10^{-4}. Neglecting the effect of gravity, the density ratio of CO_2 to water taken as 1 (i.e., $\rho_{CO_2} = \rho_{H_2O}$) has little effect on the results.[46] The contact angles θ_2 of water and the surface are 26.8°, 45.1°, 62.2°, 74.2°, 90°, 104.7°, 117.8°, 133.6°, and 153.5°, respectively.

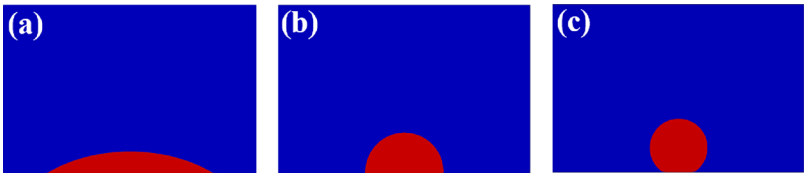

Figure 4. Interaction of two fluids with a surface: (a) $G_{ads,2}$ = −0.4, θ_2 = 26.8°; (b) $G_{ads,2}$ = 0, θ_2 = 90°; (c) $G_{ads,2}$ = 0.4, θ_2 = 153.5° (red, water; blue, CO_2).

https://doi.org/10.1021/acsomega.2c01436
ACS Omega 2022, 7, 20833−20844

In this section, the effects of the surface wettability, porosity, and granule size of porous media on the CO_2−water displacement process are discussed. The displacement efficiency is evaluated by two parameters. One is the breakthrough time of CO_2, t_b, defined as the time required for the invading fluid to reach the outlet. The other is the saturation of CO_2, S_{CO_2}, at a quasi-steady state, defined as the percentage of CO_2 in pore volume when the saturation difference of CO_2 per 10^4 iterations is less than 10^{-3}.

3.1. Effect of Surface Wettability. A series of numerical simulations are conducted to study the influence of surface wettability on the CO_2−water displacement process. The displacement process takes place in the porous media of sample 3, where the porosity and average granule size are 0.65 and 0.01, respectively.

Figure 6 shows the flow process of CO_2 (red) in pores under different surface wettability values. Approximately at $0° < \theta_2 < 75°$, the solid surface exhibits hydrophilic properties so that water is prone to adhere to the solid surface and form a liquid film. Therefore, it is easier for CO_2 to flow along the center of the pore channel. The irregularity of the porous media leads to different capillary pressures in each pore. The CO_2 front preferentially forms multiple protrusions and invades some large pore channels in porous media and also merges and separates continuously. Gradually, the dominant channels are established, known as fingering mode. Approximately at $105° < \theta_2 < 180°$, the surface exhibits hydrophobic properties, and CO_2 flows along the solid surface more easily due to the adhesion between CO_2 and the solid surface. The two-phase interface forms a concave shape and moves relatively slowly, which has a more stable invasion front than that in the hydrophilic case. When the solid surface is hydrophobic, the capillary pressure of CO_2 in the flow process is small so that it can fill large or small pore spaces more uniformly, thus forming a relatively flat invasion front. This phenomenon is also called stable displacement mode. It should also be noted that the capillary pressure of CO_2 in the process of flow decreases with the increase in contact angle, resulting in a transition pattern between the two modes. Approximately at $75° < \theta_2 < 105°$, the coexistence of the two modes is clearly observed. There is not only a relatively flat front surface locally but also a certain degree of protrusions, as also proposed in the study of Bakhshian et al.[51]

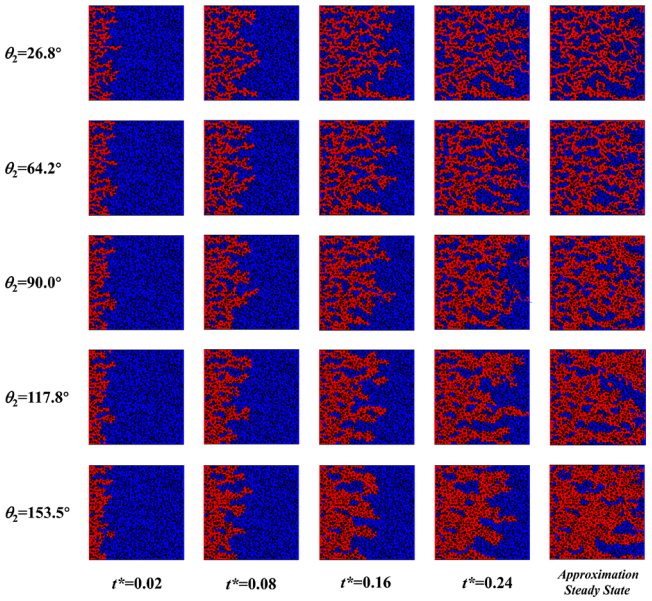

Figure 6. Distribution of CO_2 in the pore space at different times and wettability values (red, CO_2; blue, water; black, skeleton structure).

The morphological characteristics of residual water in porous media are shown in Figure 7 with different wettability values. A portion of water in the pore space is separated by CO_2 during the flow to form separate residual water masses, which exist in three types of forms. Among them, the vast majority of the residual water masses occupy both the throats and pore bodies (the first type of residual water, I), the minority of smaller residual water masses alone occupy the throats or pore bodies (the second type of residual water, II), and a very minor amount of residual water adheres to the solid surface in the form of a water film (the third type of residual water, III). Since the driving force needs to overcome the capillary pressure of the throat, the water clusters are very difficult to remobilize once trapped by CO_2 in the throats. In the hydrophilic case, for example, $\theta_2 = 26.8°$ in Figure 7a, a certain amount of CO_2 can be observed to form a continuous flow path in the form of thin and long linked large clusters. Three types of residual water exist in the porous media simultaneously. The second type of residual water exists in the throats. The reason is that CO_2, as a nonwetting phase, needs to overcome large capillary breakthrough pressure when entering the throat due to the smaller geometric width of the throat. Therefore, the nonwetting phase tends to occupy larger pores rather than the smaller ones. Unlike the pore-fluid distribution observed in the highly hydrophilic case, as shown in Figure 7b at $\theta_2 = 90°$, it depicts a wide continuous flow path of CO_2. In addition, both CO_2 and residual water can occupy the pore bodies or throats, demonstrating that the form of the second category of residual water has changed. In addition, the third type of residual water has also been observed in this case. Figure 7c shows the hydrophobic case, for example, $\theta_2 = 153.5°$, where CO_2 sweeps the flow channel in a large area, the second type of residual water only occupies the pores, and the third type of residual water is not presented.

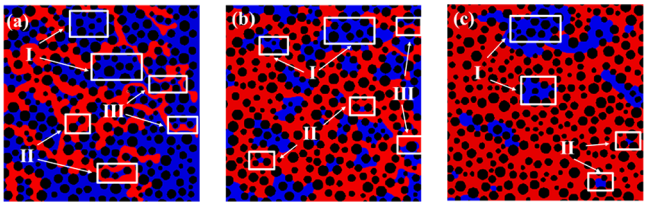

Figure 7. Three types of residual water for various wettability values: (a) $\theta_2 = 26.8°$; (b) $\theta_2 = 90.0°$; (c) $\theta_2 = 153.5°$.

Figure 8 demonstrates the variation of the CO_2 saturation in porous media over time with different wettability values. At the same contact angle, the growth process of CO_2 volume fraction can be divided into three stages: (1) rapid growth stage; (2) slow growth stage; (3) stabilization stage. In the early stage of the displacement process, the available pore space of CO_2 in the porous media is relatively large, and the saturation of CO_2 in the pores increases rapidly. When CO_2 flows out of the outlet, CO_2 flows preferentially along the dominant channel. However, CO_2 is still able to break through some small pores due to the action of viscous force, leading to a slow growth rate of its saturation. At the later stage of the displacement process,

https://doi.org/10.1021/acsomega.2c01436
ACS Omega 2022, 7, 20833−20844

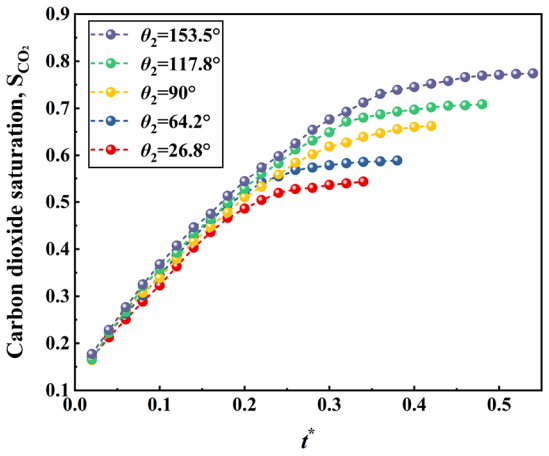

Figure 8. Relationship of CO_2 saturation with time under different wettability values.

the inflow and outflow of CO_2 are basically stable and its saturation remains steady. In addition, with the enlargement of the contact angle, the surface changes from hydrophilic to hydrophobic, and the duration of the rapid growth stage and slow growth stage increases.

As shown in Figure 9, the breakthrough time and final saturation of CO_2 with the contact angle θ_2 confirm the

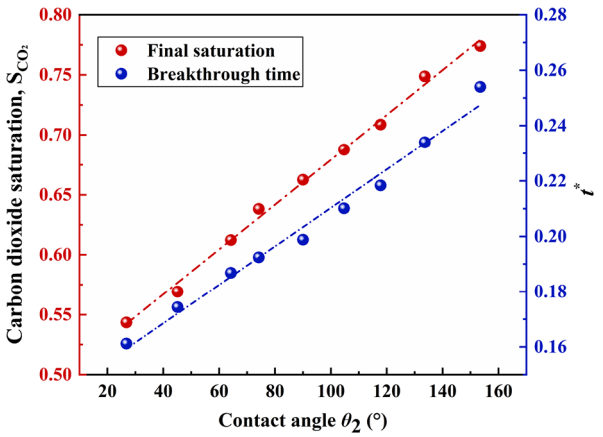

Figure 9. Final saturation and breakthrough time of CO_2 as a function of contact angle.

function relationship. The breakthrough time t^* of CO_2 prolongs with the increase in contact angle. Specifically, the breakthrough time t^* of CO_2 increases from 0.161 to 0.254 with the change of the contact angle from 26.8° to 153.5°. The final saturation of CO_2 increases with the rise of contact angle from 54.35 to 77.4%. This can be attributed to the fact that when the porous media are hydrophilic, water forms a liquid film on the wall, which acts as lubrication, thus making CO_2 flow faster and shortening the breakthrough time. The smaller the contact angle is, the much stronger the adhesion of water to the surface will be. This adhesion makes it more difficult for CO_2 to displace water, resulting in a lower CO_2 displacement efficiency. Conversely, when CO_2 is the wetting phase, it will flow close to the wall under the action of adhesion, which slows down the flow rate of CO_2 and prolongs the CO_2 breakthrough time. However, at this time, the adhesion of water to the wall is smaller, and the resistance encountered in the process of CO_2 displacing water is smaller so that CO_2 can infiltrate more pore spaces, resulting in higher saturation. Considering the final saturation as the dominant parameter, the simulation results show that improving the wettability of CO_2 with the solid surface can help improve the displacement efficiency of CO_2, demonstrating an approximately linear relationship, in good agreement with the results of Dong et al.[50]

3.2. Effect of Porosity. A series of simulations are performed by varying the porosity of porous media at different contact angles. The samples of porous media are 1, 2, 3, 4, and 5 with the same average granule size D^* of 0.01, corresponding to the porosities ε = 0.60, 0.62, 0.65, 0.68, and 0.70, respectively.

Figure 10 illustrates the distribution of CO_2 in porous media at different porosities when the displacement process reaches

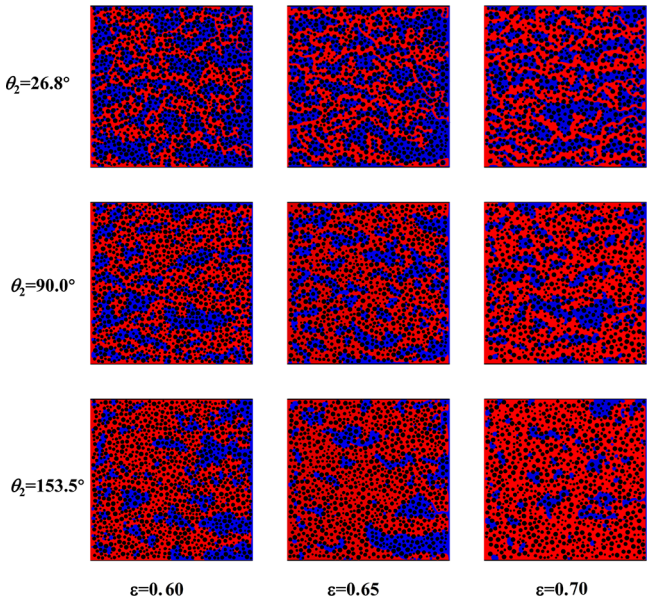

Figure 10. Distribution of CO_2 in porous media for different porosities and wettability values at the quasi-steady state with an average granule size of 0.01(red, CO_2; blue, water; black, skeleton structure).

the quasi-steady state. Under the same wettability condition θ_2, the number of dominant channels established by CO_2 in the porous media rises and the sweep area widens significantly with the porosity increasing. At the same average granule size, the porous media with larger porosity have a smaller solid surface area, providing more pore channels for two-phase fluid flow. Conversely, the flow channels in porous media with smaller porosity are narrower, while the inflow space is smaller. To sum up, with the porosity increasing, the flow becomes more continuous. Moreover, regardless of the porosity, the form of residual water in the porous media is still dominated by the first type. Also, a slight change in porosity will cause a large difference in the volume fraction of residual water in the pores.

In addition, as shown in Figure 10, for ε = 0.60, the case of θ_2 = 26.8° (hydrophilic) maintains a "fingering mode", and while the contact angle increases to 153.5° (hydrophobic), the flow pattern changes to the "stable displacement mode". The two modes coexist in the condition of neutral wetting. However, as ε increases from 0.60 to 0.70 for a fixed contact

https://doi.org/10.1021/acsomega.2c01436
ACS Omega 2022, 7, 20833−20844

angle, the displacement mode of CO_2 is not affected by the change of porosity.

Figures 11 and 12 show the porosity as a function of CO_2 breakthrough time and final saturation under different θ_2

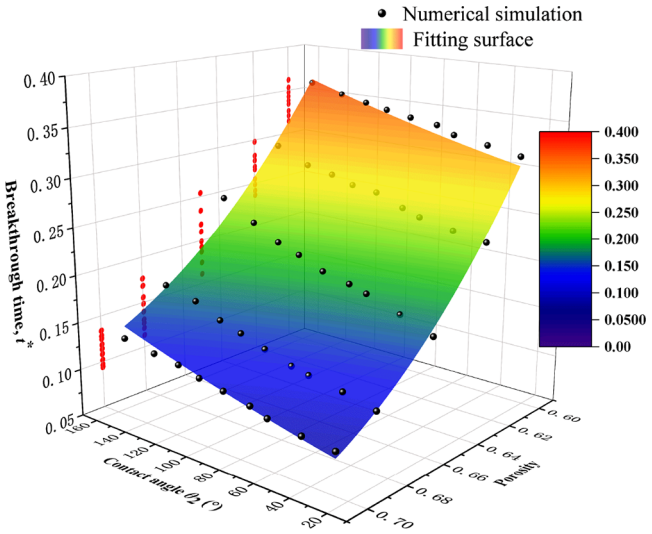

Figure 11. Relationship between CO_2 breakthrough time and porosity under different contact angles.

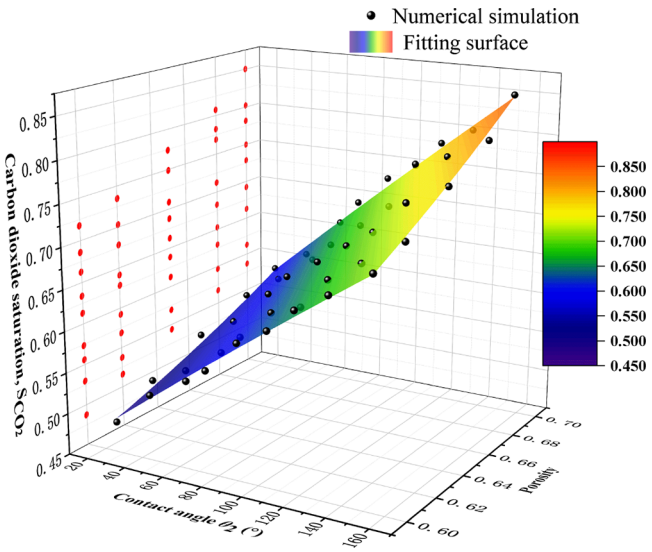

Figure 12. Relationship between the final saturation of CO_2 and porosity under different contact angles.

values. For example, at θ_2 = 26.8°, the porosity of porous media increases from 0.60 to 0.70, the breakthrough time t^* of CO_2 decreases from 0.314 to 0.094, and the final saturation increases from 48.74 to 58.63%. Similarly, when the porosity varies within the same range at θ_2 = 153.5°, the breakthrough time of CO_2 is shortened from 0.362 to 0.164, and the final saturation increases from 71.78 to 85.02%. This is because as the porosity increases for a fixed average granule size, it leads to the increase in mean pore throat size. As a result, the permeability of porous media increases significantly, and the resistance to the displacement process decreases. Therefore, the breakthrough time is shortened and the final saturation is higher.

Increasing the porosity of porous media can significantly reduce the breakthrough time and increase the final saturation of CO_2. The results show that selecting reservoirs with higher porosity is helpful in improving the CO_2 displacement efficiency.

3.3. Effect of Granule Size. The porous media with uniform granule size are the simplest model to study the effect of granule size on the displacement process, but they cannot reflect the heterogeneity of the real porous media. The non-uniform porous media have a variety of granule sizes, and the effect of granule size can be studied by controlling the overall average granule size and considering the non-uniformity of granule size, which better reflects the heterogeneity of the real situation.

3.3.1. Effect of Uniform Granule Size. The samples of porous media are 11, 12, 13, 14, and 15 with the granule sizes of 0.01, 0.012, 0.014, 0.016, and 0.018, respectively, when the porosity is 0.65. For uniform granule sizes, that is, the size of solid granules in porous media is consistent, and the effect of different granule sizes on the CO_2−water displacement process is studied.

Figure 13 illustrates the distribution of CO_2 in porous media at different granule sizes and wettability values when the

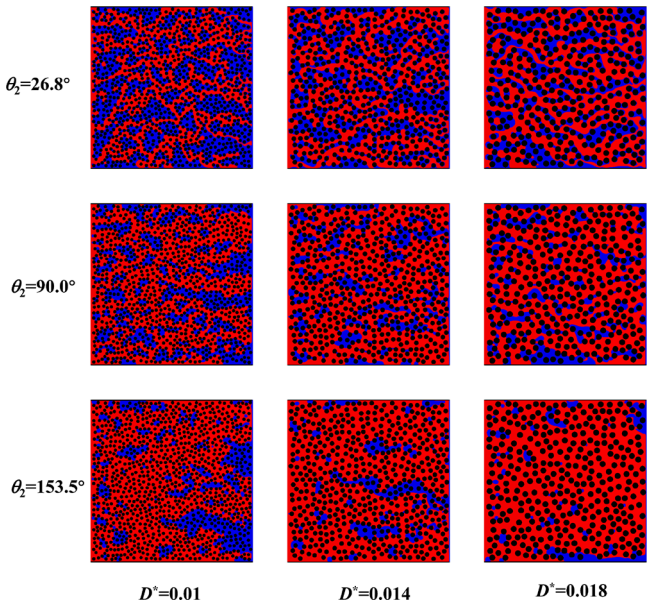

Figure 13. Distribution of CO_2 in porous media for different wettability values and granule sizes at the quasi-steady state (red, CO_2; blue, water; black, skeleton structure) with a porosity of 0.65.

displacement process reaches the quasi-steady state. When θ_2 = 26.8° and D^* = 0.01, much CO_2 flows along the surface, which causes the water film on the surface to be very thin or even disappear, and CO_2 penetrates water along the center of the flow path only in part of the pores. In addition, in the flow process, it can be found that CO_2 breaks through a few small throats and is subjected to a large capillary pressure. As the average granule size increases, for example, when D^* = 0.018 for the fixed contact angle, it can be clearly observed from the figure that there are thick water films between the surface and CO_2 in several places, and CO_2 flows through the water layer along the center in several flow channels. The reason is that on the premise of the same wettability and porosity, the seepage network in the porous media with small granule size is

https://doi.org/10.1021/acsomega.2c01436
ACS Omega 2022, 7, 20833−20844

characterized by numerous exceedingly fine seepage channels; in addition, the proportion of main channels is low, and each channel is distorted.

From the results shown in Figure 13, it can be clearly observed that the residual water morphology is still dominated by the first type. The volume fraction of the first and second types of residual water can be significantly reduced by increasing the size of solid granules in porous media, but the volume fraction of the third type of residual water increases. However, the increase in the volume fraction of the third type of residual water is extraordinarily smaller compared to the decrease in the volume fraction of the first and second ones of residual water.

In the case of D^* = 0.01 and θ_2 = 26.8°, the porous media maintain a "fingering pattern". Meanwhile, when θ_2 = 153.5°, the CO_2 displacement mode changes to the "stable displacement pattern". The coexistence of the two modes can clearly be captured in the condition of neutral wetting. As D^* increases from 0.01 to 0.018, the displacement mode of CO_2 remains unchanged under the same wettability. The results show that the granule size has no effect on CO_2 displacement mode in porous media.

Figures 14 and 15 show the CO_2 breakthrough time and final saturation as a function of granule size under different θ_2 values. At θ_2 = 26.8°, the granule size D^* increases from 0.01 to 0.018, the breakthrough time of CO_2 is shortened from 0.168 to 0.05, and the saturation increases from 49.21 to 65.6%. At θ_2 = 153.5°, when the granule size changes within the same range, the breakthrough time of CO_2 is shortened from 0.283 to 0.073, and the saturation increases from 74.83 to 89.11%. When θ_2 changes from 26.8° to 153.5°, the saturation values of CO_2 increase by 25.62% for D^* = 0.01, 24.18% for D^* = 0.014, and 23.51% for D^* = 0.018. The results show that under the same wettability, the breakthrough time of CO_2 is an approximately quadratic function, and the final saturation of CO_2 is linear with the granule size. The reason is that as the granule size increases, the channel becomes wider and straighter, the resistance of CO_2 during the flow process in porous media is reduced, and the flow velocity becomes faster, so the time to reach the outlet is shortened and the final saturation is higher.

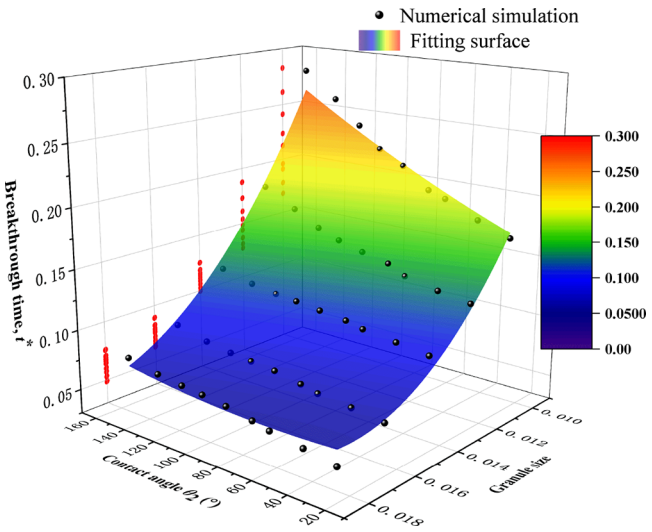

Figure 14. Relationship between CO_2 breakthrough time and granule size under different contact angles.

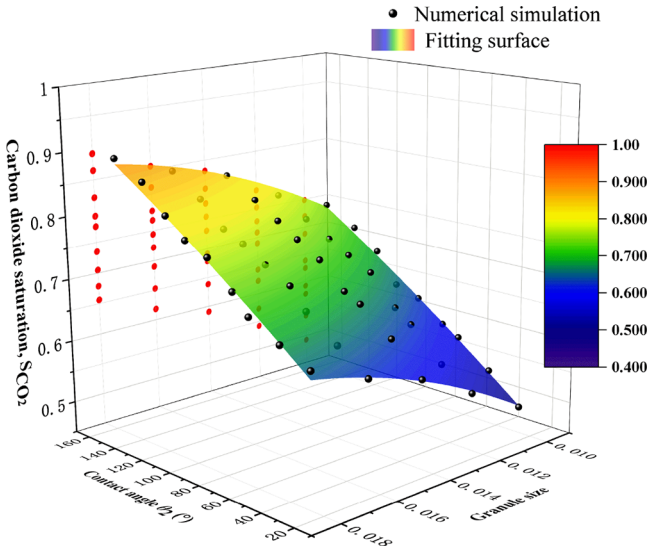

Figure 15. Relationship between the final saturation of CO_2 and granule size under different contact angles.

As the granule size increases, the breakthrough time of CO_2 is significantly shortened and the final saturation increases. Moreover, compared with the number of flow channels in uniform porous media, the displacement efficiency of CO_2 is more sensitive to the width of the flow channels. Also, in the case of the same flow channel width, as the contact angle increases, the displacement efficiency of CO_2 increases.

3.3.2. Effect of Non-uniform Granule Size. In the study of Section 3.3.1, the granule size in the same porous media is consistent. In this section, we consider the case of non-uniform granule size, which is of multiple granules with different sizes in the same porous media. But it is ensured that the porosity and average size of the granules of the porous media are 0.65 and 0.01, respectively, consistent with the parameters used in Section 3.3.1, to study the influence of the non-uniformity of porous media on the CO_2−water displacement process. The porous media samples are 3, 7, 8, 9, and 10, with the average size ranging from 0.01 to 0.018.

Figure 16 illustrates the distribution of CO_2 in porous media at different average granule sizes when the displacement process reaches the quasi-steady state in the case of non-uniform granules. Comparing Figures 13 and 16, we find that under any fixed wettability, the morphological characteristics of residual water are consistent regardless of the granule size and average granule size for the flow characteristics of the displacement process, but the flow of CO_2 in non-uniform porous media is more continuous than that in uniform ones. As shown in Figure 16, at θ_2 = 26.8°, it can be clearly observed that the main channel of CO_2 is basically established along the vicinity of the large granule size, while the small granule size only disturbs the flow of the main channel. At θ_2 = 153.5°, the distribution of CO_2 in non-uniform porous media is more uniform, and the volume fraction of CO_2 adsorbed on the solid surface around the smaller pores is significantly reduced. The reason that can be described is that the non-uniformity of granule size affects the flow channel morphology so that large pores and wider channels appear near the large-size granule, and the resistance of CO_2 during the flow is reduced.

https://doi.org/10.1021/acsomega.2c01436
ACS Omega 2022, 7, 20833−20844

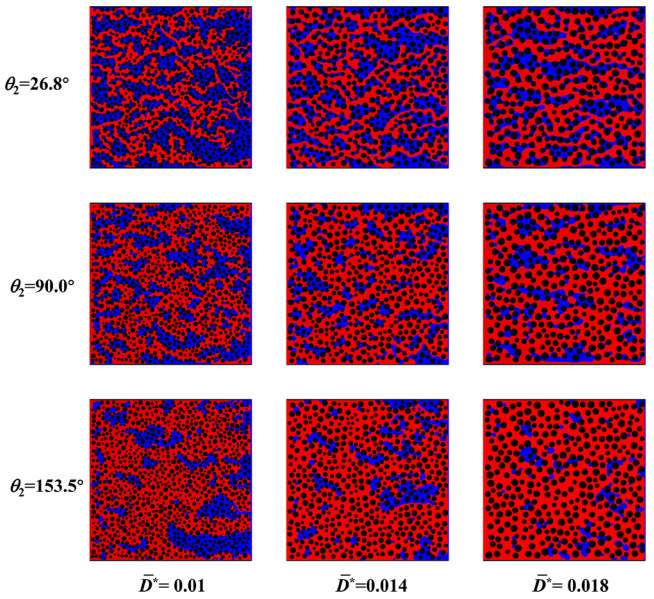

Figure 16. Distribution of CO_2 in non-uniform porous media for different wettability values and average sizes of solid granules at the quasi-steady state (red, CO_2; blue, water; black, skeleton structure) with a porosity of 0.65.

As shown in Figures 17 and 18, in non-uniform porous media, the breakthrough time of CO_2 and the average granule

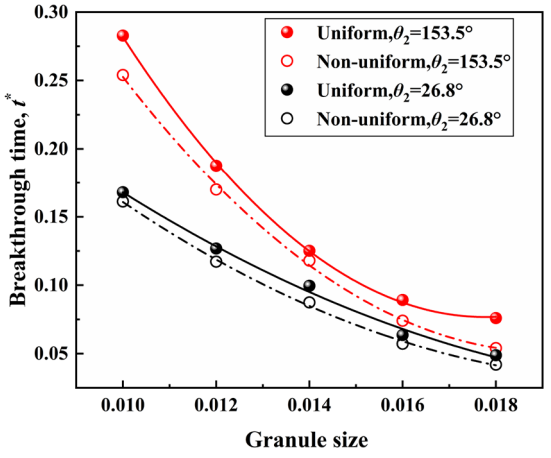

Figure 17. Relationship between CO_2 breakthrough time and average granule size under different contact angles.

size still conform to the law of quadratic function, and the final saturation presents a nearly linear relationship. It is also found that the breakthrough time of CO_2 in non-uniform porous media is shorter, and the final saturation is higher than those in uniform porous media for other factors fixed. The reason is that the proportion of wider flow channels in non-uniform porous media increases relative to uniform porous media, and CO_2 tends to flow preferentially along these flow channels; therefore, the time to reach the outlet is shortened and the final saturation is higher. In summary, the non-uniformity of porous media can improve the CO_2 displacement efficiency.

3.3.3. Effect of Non-uniformity of Granule Size. From the results in Section 3.3.2, we find that although the average granule size of the porous media is the same, the non-uniformity of granule size seems to have a certain impact on

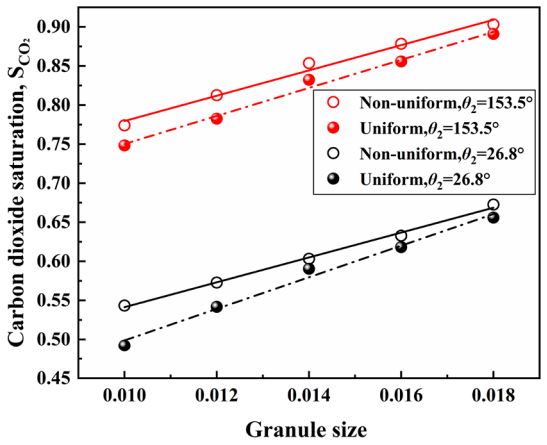

Figure 18. Relationship between the final saturation of CO_2 and average granule size under different contact angles.

the displacement process and efficiency. In this section, we ensure that the porosity and average granule size of the porous media are consistent, $\varepsilon = 0.65$ and $\bar{D}^* = 0.01$, respectively. To quantificationally study the effect of the non-uniformity of granule size, the standard deviation is applied using $\kappa = \sqrt{\frac{1}{n}\left(\sum_{i=1}^{n}(D^* - \bar{D}^*)^2\right)}$, where n is the total number of granules. The standard deviations of porous media samples 11, 3, and 6 are calculated as 0, 1.284, and 2.168, respectively. The influence of the standard deviation (i.e., non-uniformity) of the porous media on the displacement process and efficiency is discussed.

Figure 19 shows the distribution of CO_2 in porous media under different standard deviations in the quasi-steady state at

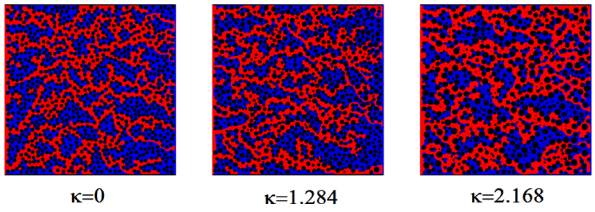

Figure 19. Distribution of CO_2 in non-uniform porous media under different standard deviations in the quasi-steady state at $\theta_2 = 26.8°$ (red, CO_2; blue, water; black, skeleton structure), with a porosity of 0.65 and an average granule size of 0.01.

$\theta_2 = 26.8°$. With the further expansion of the standard deviation, it can be clearly found that the CO_2 channel is still established in the vicinity of the large-size granules, the flow of CO_2 is more continuous, and the large-area residual water is reduced. However, the seepage network characteristics of CO_2 in porous media have a great difference, embodied in the width and number of main channels. The reason is that as the standard deviation increases, the distribution of solid granules becomes more and more uneven. Therefore, the number of large-size granules increases, resulting in the increasing proportion of a wider flow channel, and the number of small-size granules increases, leading to the weakened or even disappearing disturbance effect on the flow channel of CO_2.

We quantify the breakthrough time and final saturation of CO_2 to illustrate the impact of granule unevenness on displacement efficiency as shown in Figures 20 and 21. As the standard deviation increases, the breakthrough time is

https://doi.org/10.1021/acsomega.2c01436
ACS Omega 2022, 7, 20833−20844

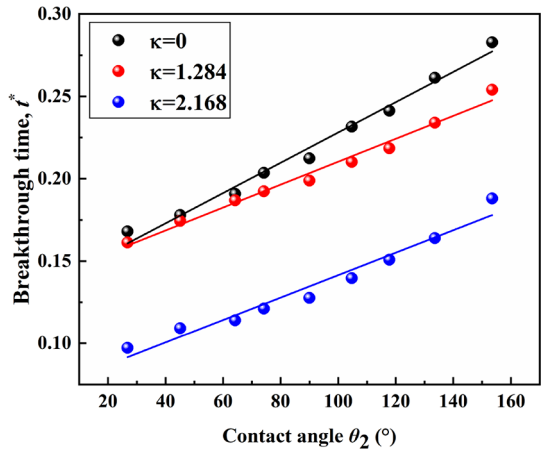

Figure 20. Relationship between the final saturation of CO_2 and wettability under different standard deviations.

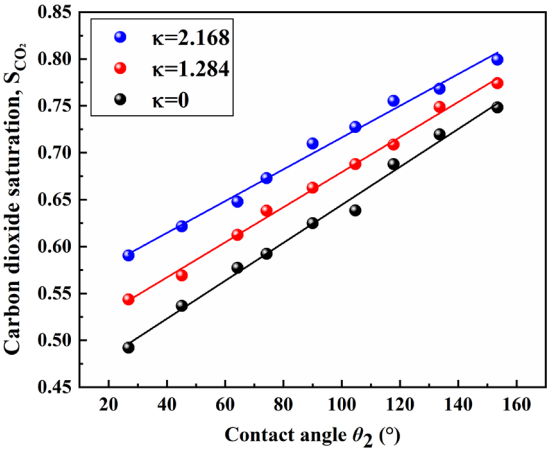

Figure 21. Relationship between the breakthrough of CO_2 and wettability under different standard deviations.

significantly shortened and the final saturation increases. For example, at θ_2 = 26.8°, with increasing standard deviation from 0 to 2.168, the breakthrough time is shortened from 0.168 to 0.097, and the final saturation increases from 49.21 to 59.04%. The results show that choosing a reservoir with a greater non-uniformity of granule size is beneficial to improve the efficiency of CO_2 displacement.

4. CONCLUSIONS

In this paper, based on two-dimensional heterogeneous porous media models numerically reconstructed with different porosities and granule sizes, the immiscible two-phase CO_2–water displacement process at the pore scale is simulated by the LBM method, and the displacement efficiency is evaluated under different conditions. It is concluded as follows:

With the enhancement of CO_2-surface wettability representing the fluid–solid interaction, the CO_2 displacement mode changes from fingering to stable displacement, where residual water tends to occupy the pores instead of the throats, and the saturation of CO_2 at the quasi-steady state increases significantly. Although the breakthrough time becomes longer, the overall displacement efficiency shows a trend of improvement.

For the porous media characteristic factors, with the increase in porosity, granule size, and non-uniformity of granule size in the heterogeneous porous media, the sweeping area of the CO_2 mainstream channel increases and the flow becomes more continuous, where the breakthrough time of CO_2 is shortened, the final saturation at the quasi-steady state increases significantly, and the displacement efficiency shows a trend of improvement.

In summary, wettability is the primary mechanism to improve CO_2 displacement efficiency. Even if porous media maintain a low porosity or small average granule size, CO_2 can still maintain a high displacement efficiency in hydrophobic porous media. The reservoirs with high porosity, large granule size, and great non-uniformity of granule size have greater storage capacity, which can help improve the geological storage efficiency of CO_2.

AUTHOR INFORMATION

Corresponding Author

Ling Ren – *Department of Thermal Science and Energy Engineering, University of Science and Technology Beijing, Beijing 100083, China*; Email: renl@me.ustb.edu.cn

Authors

Qi Liu – *Department of Thermal Science and Energy Engineering, University of Science and Technology Beijing, Beijing 100083, China*; orcid.org/0000-0002-8157-6436

Yang Ni – *Department of Thermal Science and Energy Engineering, University of Science and Technology Beijing, Beijing 100083, China*

Yucong Xia – *Department of Thermal Science and Energy Engineering, University of Science and Technology Beijing, Beijing 100083, China*

Jianguo Chen – *Department of Engineering Physics, Tsinghua University, Beijing 100084, China*

Complete contact information is available at: https://pubs.acs.org/10.1021/acsomega.2c01436

Notes

The authors declare no competing financial interest.

ACKNOWLEDGMENTS

The authors would like to express their gratitude for the project supported by the National Natural Science Foundation of China (fund no. 71861167002).

REFERENCES

(1) Surridge, A. D.; Cloete, M. Carbon capture and storage in South Africa. *Energy Procedia* **2009**, *1*, 2741–2744.

(2) Soltanian, M. R.; Amooie, M. A.; Cole, D. R.; Graham, D. E.; Hosseini, S. A.; Hovorka, S.; Pfiffner, S. M.; Phelps, T. J.; Moortgat, J. Simulating the Cranfield geological carbon sequestration project with high-resolution static models and an accurate equation of state. *Int. J. Greenhouse Gas Control* **2016**, *54*, 282–296.

(3) Er, V.; Babadagli, T.; Xu, Z. Pore-scale investigation of the Matrix-Fracture interaction during CO_2 injection in naturally fractured oil reservoirs. *Energy Fuels* **2010**, *24*, 1421–1430.

(4) Bachu, S. Screening and ranking of sedimentary basins for sequestration of CO_2 in geological media in response to climate change. *Environ. Geol.* **2003**, *44*, 277–289.

(5) Bakhshian, S.; Sahimi, M. Adsorption-induced swelling of porous media. *Int. J. Greenhouse Gas Control* **2017**, *57*, 1–13.

(6) Hosseini, S. A.; Nicot, J. Numerical modeling of a multiphase water–oil-CO_2 system using a water–CO_2 system: Application to the far field of a U.S. Gulf Coast reservoir. *Int. J. Greenhouse Gas Control* **2012**, *10*, 88–99.

https://doi.org/10.1021/acsomega.2c01436
ACS Omega 2022, 7, 20833–20844

(7) Chapman, D. A.; Lickel, B. Climate Change and Disasters. *Soc. Psychol. Pers. Sci.* **2016**, *7*, 13−20.
(8) Kazemifar, F.; Kyritsis, D. C. Experimental investigation of near-critical CO_2 tube-flow and Joule−Thompson throttling for carbon capture and sequestration. *Exp. Therm. Fluid Sci.* **2014**, *53*, 161−170.
(9) Zhang, C.; Oostrom, M.; Grate, J. W.; Wietsma, T. W.; Warner, M. G. Liquid CO_2 displacement of water in a dual-permeability pore network micromodel. *Environ. Sci. Technol.* **2011**, *45*, 7581−7588.
(10) Zhang, C.; Oostrom, M.; Wietsma, T. W.; Grate, J. W.; Warner, M. G. Influence of viscous and capillary forces on immiscible fluid displacement: pore-scale experimental study in a water-wet micromodel demonstrating viscous and capillary fingering. *Energy Fuels* **2011**, *25*, 3493−3505.
(11) Liu, Z.; Wu, H. Pore-scale modeling of immiscible two-phase flow in complex porous media. *Appl. Therm. Eng.* **2016**, *93*, 1394−1402.
(12) Chen, Y.; Li, Y.; Valocchi, A. J.; Christensen, K. T. Lattice Boltzmann simulations of liquid CO_2 displacing water in a 2D heterogeneous micromodel at reservoir pressure conditions. *J. Contam. Hydrol.* **2018**, *212*, 14−27.
(13) Zhu, G.; Yao, J.; Li, A.; Sun, H.; Zhang, L. Pore-scale investigation of carbon dioxide-enhanced oil recovery. *Energy Fuels* **2017**, *31*, 5324−5332.
(14) An, S.; Erfani, H.; Godinez Brizuela, O. E.; Niasar, V. Transition from viscous fingering to capillary fingering: application of GPU-Based fully implicit dynamic pore network modeling. *Water Resour. Res.* **2020**, *56*, DOI: 10.1029/2020WR028149.
(15) Zhao, J.; Kang, Q.; Yao, J.; Viswanathan, H.; Pawar, R.; Zhang, L.; Sun, H. The effect of wettability heterogeneity on relative permeability of two-phase flow in Porous Media: A Lattice Boltzmann Study. *Water Resour. Res.* **2018**, *54*, 1295−1311.
(16) Iglauer, S.; Pentland, C. H.; Busch, A. CO_2 wettability of seal and reservoir rocks and the implications for carbon geo-sequestration. *Water Resour. Res.* **2015**, *51*, 729−774.
(17) Mora, P.; Morra, G.; Yuen, D. A.; Juanes, R. Optimal wetting angles in lattice Boltzmann simulations of viscous fingering. *Transp. Porous Media* **2021**, *136*, 831−842.
(18) Jung, M.; Brinkmann, M.; Seemann, R.; Hiller, T.; Sanchez De La Lama, M.; Herminghaus, S. Wettability controls slow immiscible displacement through local interfacial instabilities. *Phys. Rev. Fluids* **2016**, *1*, No. 074202.
(19) Geistlinger, H.; Zulfiqar, B. The impact of wettability and surface roughness on fluid displacement and capillary trapping in 2-D and 3-D porous media: 1. Wettability-Controlled phase transition of trapping efficiency in glass beads packs. *Water Resour. Res.* **2020**, *56*, DOI: 10.1029/2019WR026826.
(20) Xie, Q.; Chen, Y.; Sari, A.; Pu, W.; Saeedi, A.; Liao, X. A pH-Resolved wettability alteration: implications for CO_2-Assisted EOR in carbonate reservoirs. *Energy Fuels* **2017**, *31*, 13,593−13,13599.
(21) Hu, Z.; Azmi, S. M.; Raza, G.; Glover, P. W. J.; Wen, D. Nanoparticle-assisted water-flooding in Berea sandstones. *Energy Fuels* **2016**, *30*, 2791−2804.
(22) Li, R.; Jiang, P.; Gao, C.; Huang, F.; Xu, R.; Chen, X. Experimental investigation of Silica-Based nanofluid enhanced oil recovery: the effect of wettability alteration. *Energy Fuels* **2017**, *31*, 188−197.
(23) Hendraningrat, L.; Torsæter, O. Effects of the initial rock wettability on Silica-Based nanofluid-enhanced oil recovery processes at reservoir temperatures. *Energy Fuels* **2014**, *28*, 6228−6241.
(24) Zakirov, T. R.; Khramchenkov, M. G. Wettability effect on the invasion patterns during immiscible displacement in heterogeneous porous media under dynamic conditions: A numerical study. *J. Pet. Sci. Eng.* **2021**, *206*, No. 109049.
(25) Riazi, M.; Sohrabi, M.; Bernstone, C.; Jamiolahmady, M.; Ireland, S. Visualisation of mechanisms involved in CO_2 injection and storage in hydrocarbon reservoirsand water-bearing aquifers. *Chem. Eng. Res. Des.* **2011**, *89*, 1827−1840.
(26) Zakirov, T. R.; Khramchenkov, M. G. Characterization of two-phase displacement mechanisms in porous media by capillary and viscous forces estimation using the lattice Boltzmann simulations. *J. Pet. Sci. Eng.* **2020**, *184*, No. 106575.
(27) Yang, W.; Chang, Y.; Cheng, J.; Wang, Z.; Li, X.; Lv, P.; Zhang, B.; Wang, L.; Liu, B.; Song, Y. Effects of pore structures on seepage and dispersion characteristics during CO_2 miscible displacements in unconsolidated cores. *Energy Fuels* **2021**, *35*, 17791−17809.
(28) Zhao, Y.; Song, Y.; Liu, Y.; Liang, H.; Dou, B. Visualization and measurement of CO_2 flooding in porous media using MRI. *Ind. Eng. Chem. Res.* **2011**, *50*, 4707−4715.
(29) Shams, M.; Raeini, A. Q.; Blunt, M. J.; Bijeljic, B. A study to investigate viscous coupling effects on the hydraulic conductance of fluid layers in two-phase flow at the pore level. *J. Colloid Interface Sci.* **2018**, *522*, 299−310.
(30) Rokhforouz, M. R.; Akhlaghi Amiri, H. A. Effects of grain size and shape distribution on pore-scale numerical simulation of two-phase flow in a heterogeneous porous media. *Adv. Water Resour.* **2019**, *124*, 84−95.
(31) Ju, Y.; Gong, W.; Chang, W.; Sun, M. Effects of pore characteristics on water−oil two-phase displacement in non-homogeneous pore structures: A pore-scale lattice Boltzmann model considering various fluid density ratios. *Int. J. Eng. Sci.* **2020**, *154*, No. 103343.
(32) Chen, L.; Kang, Q.; Robinson, B. A.; He, Y. L.; Tao, W. Q. Pore-scale modeling of multiphase reactive transport with phase transitions and dissolution-precipitation processes in closed systems. *Phys. Rev. E* **2013**, *87*, 43306.
(33) Huang, H.; Thorne, D. J.; Schaap, M. G.; Sukop, M. C. Proposed approximation for contact angles in Shan-and-Chen-type multicomponent multiphase lattice Boltzmann models. *Phys. Rev. E* **2007**, *76*, 66701.
(34) Parmigiani, A.; Huber, C.; Bachmann, O.; Chopard, B. Pore-scale mass and reactant transport in multiphase porous media flows. *J. Fluid Mech.* **2011**, *686*, 40−76.
(35) Varotsos, P. A.; Sarlis, N. V.; Skordas, E. S. Remarkable changes in the distribution of the order parameter of seismicity before mainshocks. *Europhys. Lett.* **2012**, *100*, 39002.
(36) Shan, X.; Chen, H. Lattice Boltzmann model for simulating flows with multiple phases and components. *Phys. Rev. E* **1993**, *47*, 1815−1819.
(37) Shan, X.; Chen, H. Simulation of nonideal gases and liquid−gas phase transitions by the lattice Boltzmann equation. *Phys. Rev. E.* **1994**, *49*, 2941−2948.
(38) Guo, Z.; Shi, B.; Zheng, C. Chequerboard effects on spurious currents in the lattice Boltzmann equation for two-phase flows. *Phil. Trans. R. Soc. A* **2011**, *369*, 2283−2291.
(39) Nourgaliev, R. R.; Dinh, T. N.; Theofanous, T. G.; Joseph, D. The lattice Boltzmann equation method: theoretical interpretation, numerics and implications. *Int. J. Multiphas. Flow* **2003**, *29*, 117−169.
(40) Shan, X. Analysis and reduction of the spurious current in a class of multiphase lattice Boltzmann models. *Phys. Rev. E* **2006**, *73*, 47701.
(41) He, X.; Luo, L. Theory of the lattice Boltzmann method: from the Boltzmann equation to the lattice Boltzmann equation. *Phys. Rev. E* **1997**, *56*, 6811−6817.
(42) Shan, X.; Doolen, G. Diffusion in a multicomponent lattice Boltzmann equation model. *Phys. Rev. E* **1996**, *54*, 3614−3620.
(43) Shan, X.; Doolen, G. Multicomponent lattice-Boltzmann model with intergranular interaction. *J. Stat. Phys.* **1995**, *81*, 379−393.
(44) Zou, Q.; He, X. On pressure and velocity boundary conditions for the lattice Boltzmann BGK model. *Phys. Fluids* **1997**, *9*, 1591−1598.
(45) Hecht, M.; Harting, J. Implementation of on-site velocity boundary conditions for D3Q19 lattice Boltzmann simulations. *J. Stat. Mech.: Theory Exp.* **2010**, *2010*, P1018.
(46) Succi, S.; Foti, E.; Higuera, F. Three-dimensional flows in complex geometries with the lattice Boltzmann method. *Europhys. Lett.* **1989**, *10*, 433−438.
(47) Liu, H.; Valocchi, A. J.; Werth, C.; Kang, Q.; Oostrom, M. Pore-scale simulation of liquid CO_2 displacement of water using a

two-phase lattice Boltzmann model. *Adv. Water Resour.* **2014**, *73*, 144−158.
(48) Shi, Y.; Tang, G. H. Relative permeability of two-phase flow in three-dimensional porous media using the lattice Boltzmann method. *Int. J. Heat Fluid Fl.* **2018**, *73*, 101−113.
(49) Huang, H.; Sukop, M. C.; Lu, X. Multiphase lattice Boltzmann methods: theory and application. *Wiley Blackwell.* 2015.
(50) Dong, B.; Yan, Y. Y.; Li, W. Z.; Song, Y. C. Simulation of the influence of surface wettability on viscous fingering phenomenon in porous media. *J. Bio. Eng.* **2010**, *7*, 267−275.
(51) Bakhshian, S.; Rabbani, H. S.; Shokri, N. Physics-Driven investigation of wettability effects on two-phase flow in natural porous media: recent advances, new insights, and future perspectives. *Transp. Porous Media* **2021**, *140*, 85−106.

https://doi.org/10.1021/acsomega.2c01436
ACS Omega 2022, 7, 20833−20844